Macroscopic and microscopic trans-scale characteristics of the pore structure of mine grouting materials

Jian-hua HU[1], Qi-fan REN[1], Shao-wei MA[1], Quan JIANG[1], Yuan-jian JIANG[1], Jun-long SHANG[2], Zhou-quan LUO[1]

1.College of resources and safety engineering, Central South University, Changsha 410083, China

2.Nanyang Centre for Underground Space, School of Civil and Environmental Engineering, Nanyang Technological University, Singapore

Abstract: This paper presents a laboratory description of the microstructure of grouting materials in terms of pore structure and interconnectivity. The pore structure was characterized based on a thin-section analysis and low-field nuclear magnetic resonance (NMR) technique. The macroscopic pore interconnectivity was investigated using binary images captured from thin sections and a random walk pore spectral dimension (RWPSD) algorithm. The experimental results show that: (1) The microstructure of the grouting materials used in the study consisted of interlayer pores, gel pores, capillary pores, circular air holes, and fractures and tailings can fill some gaps in the hydration product structure and dense hydration products. (2) There is a positive correlation between pore interconnectivity and curing time. In addition, there is a relationship between pore interconnectivity and porosity. (3) A non-uniform pore structure with increasing porosity and pore interconnectivity with an accelerator result in reduced setting time and reduced later strength.

Keywords: Grouting material; Microstructure; Trans-scale study; Nuclear magnetic resonance (NMR); Thin-section analysis; Random walk pore spectral dimension (RWPSD)

1. Introduction

The development of an environmental friendly, high performance grouting material based on recycling of industrial waste is an important goal in the future[1,2]. The use of tailings in grouting not only allows tailings to be reused but can also extend the service life of tailing dams and generate additional economic and environmental benefits. Grouting materials require a short setting time and certain ability to resist differential pressure. The microstructure of grouting materials influences its mechanical properties. Unlike conventional materials, it is the pore structure that controls flow capacity in grouting materials, rather than total porosity [3]. Therefore, a precise description and characterization of the pore system are essential for understanding the permeability and performance of grouting materials [4]. The addition of accelerators will shorten the setting time, but it is also necessary to understand the effect of accelerators and the pore structure distribution (PSD) on other material properties of grout materials [5]. In addition, the setting time and strength of grouting material must be characterized to investigate the relationship between the setting time, strength, and failure mechanism for various curing times and pore systems [6]. The pore system and pore connectivity of grouting materials is difficult to characterize because of the great complexity, which is attributed to various pore sizes, complex ingredients, inhomogeneity, and strong

Foundation item: Project (41672298) supported by the National Natural Science Foundation of China; Project (2017YFC0602901) supported by the National Key Research and Development Program of China;

Corresponding author: Shao-wei MA; Tel: +86-18535810016; E-mail: mashaowei@csu.edu.cn;

heterogeneity [7]. At present, few studies have focused on the characteristics of tailing cement slurry in water environment, there is still much work to be done.

Many techniques have been applied to investigate the pore characteristics of concrete materials in previous studies, such as environmental scanning microscopy [8], X-ray computer tomography scanning [9], nuclear magnetic resonance (NMR) [10], scanning electron microscopy(SEM) [11], and mercury intrusion porosimetry (MIP) [12]. Among these, NMR has become a widely used analytic tool to estimate the physical properties, study the pore structure, and quantify the full-range pore throat structures of rocks without destroying the material as it can provide reliable PSD information [13]. Furthermore, NMR experiments were performed on core plugs in the laboratory to provide guidance for the construction of petrophysical models, showing that the application of NMR for pore structure characterization is useful [14].

Microscopic images can be very useful for examining the pore structure of a grouting material [15]. The field of view in SEM is very small, thus the overall appearance cannot be visually observed, and the definition of a pore in the image is ambiguous. Polarization microscopy (PM) is often used to observe the mineral phase [16], and others have used this technique to examine the pore structure in grouting materials. Using PM to observe a dark area of the grouting material allows examination of the pore structure inside the material, and a wide range of pore structure information can be obtained.

Fractal theory has been considered as an effective method to characterize the complex pore structure in porous materials [17,18]. However, there are only a few studies related to the fractal characteristics of pore interconnectivity in grouting materials using NMR experiments. RWPSD is a branch of fractal theory that can be used to quantify complex pore interconnectivity using a pore spectral dimension d_s [19,20]. A series of problems remain unsolved, such as the relationship between pore spectral dimension and curing time in different grouting materials, and the influence of cement, accelerators, or tailings on pore interconnectivity. Therefore, determining the pore spectral dimension in PM images can provide a new understanding of the pore network in grouting materials.

In this paper, we investigated the microstructure (in terms of pore structure and interconnectivity) and its relationship to mechanical properties (with respect to UCS and setting time) in three types of grouting materials. First, we analyzed mineral compositions and physical properties. Then the ratio of materials including cement, tailings, and water was determined, and samples were prepared and cured. The relationship between composition, setting time, and UCS was also investigated. NMR and a thin section analysis with PM were used to obtain pore structure characteristics and porosity information on the three types of grouting materials during curing time (in terms of pore structure characteristics and porosity). A macroscopic

characteristic of pore interconnectivity within the three grouting materials was quantified using the binary image PM technique and RWPSD algorithm. PSD and porosity in the three types of grouting materials obtained from NMR and image analysis of the thin-section were compared and discussed. UCS (with respect to strength failure mechanism), PSD and setting time (with respect to effects of accelerator) were investigated and the relationship between was discussed.

2. Materials and methodology

2.1 Sample preparation

Portland cement was provided by the Changsha Pingtang Cement Co., Ltd. Industrial water-glass with 40Be′ Baume degree and 2~2.4 modulus was prepared as an accelerator. In addition, potable municipal water was used to prepare the mixtures.

The tailings used in this study (Fig. 1a) were collected from the Dongan Xinlong mine tailings reservoir located in Yongzhou City, Hunan Province (China). Fig. 1b presents the cumulative grain-size distribution curve determined using a Malvern® Mastersizer S2000 laser particle size analyzer. From this figure, 80% of tailings are coarse (d > 75μm) grains. The chemical composition of the tailings was analyzed using inductively coupled plasma atomic emission spectroscopy (ICP-AES, Optima 3000 DV, Perkin-Elmer) in Table 1. The specific gravity Gs of the tailings was determined to be 2.72 using a helium pycnometer (AccuPyc 1330 from Micrometrics®) in accordance with the ASTM C128 standard.

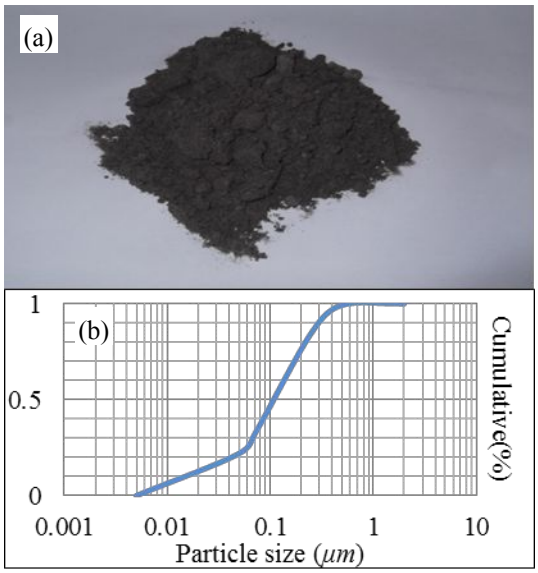

Fig. 1 Tailing appearance and cumulative grain size distribution curve for Dongan Xinlong mine (DXM) tailings.

Low-field NMR imaging and a thin-section analysis were performed on three different sample groups:

(a) Principal paste: Water-solid (w/s) ratio of 2 and with a Portland cement content of 100 wt. % (named C100);

(b) Principal paste: Water-solid (w/s) ratio of 0.5 and with a Portland cement content of 100 wt. %. The radio of principal paste volume to water-glass paste volume is 0.5 (named C100WG);

(c) Principal paste: Water-solid (w/s) ratio of 0.5 and with a mix of 50 wt. % Portland cement and 50 wt. % tailings. The ratio of principal paste volume to water-glass paste volume is 0.5 (named C50WG).

Table 1 Chemical composition of Dongan Xinlong mine tailings.

oxide	Al_2O_3	SiO_2	Fe_2O_3	CaO	MgO
Wt/%	1.943	79.97	1.434	3.569	2.513

The preparation of C50WG, C100, and C100WG specimens are as follows:

The principal paste was thoroughly stirred, and the principal paste and water-glass paste were injected into the mixer. The mixed paste was poured into cylindrical plastic molds (50.8 mm diameter and 101.6 mm height), sealed, and left in a humidity chamber for prescribed curing times (3, 7, 14, and 28 days). The samples were examined using PM and low-field NMR at 23 °C and 90% relative humidity.

2.2 Experiments

Fig. 2 shows the experiment process, including sample preparation, nuclear magnetic resonance (NMR) experiment, uniaxial compressive strength (USC) tests, and polarization microscopy (PM) examination. The setting time of C100, C100WG, and C50WG pastes was investigated.

Three cylindrical samples for each mixture were used to measure UCS after 3, 7, 14, and 28 day curing times (i.e., five tests for each recipe), according to ASTM D2166M-16. UCS tests were conducted and the setting time was measured under the same experimental conditions and mixture ratio.

Low field NMR measurements were performed using an AniMR-150 NMR analysis meter. After curing for 3, 7, 14, or 28 days, four sets of NMR measurements were gathered at 100% water saturated conditions. In this study, the T_2 distribution curves and parameters such as NMR porosity were determined in water saturated conditions.

Due to the poor strength of the specimens, it was necessary to use plastics before conducting a thin-section analysis. Epoxy resin and triethanolamine (ratio 9:1) were heated on an electric furnace until the mixture began boiling, and the sample was subsequently placed in the mixture and boiled for 3 to 5 minutes.

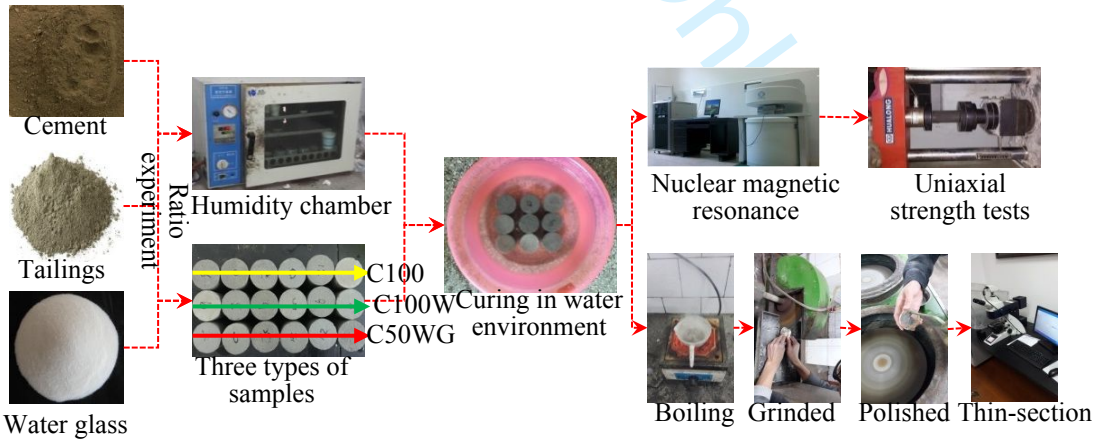

Fig. 2 Experimental process with sample preparation, NMR experiment, USC test, and PM examination.

The sample was ground and polished after boiling. Potassium dichromate and chromium oxide (ratio of 3:7) with a factor 40 water dilution was used as the polishing agent. A microscope (DM-4500P, Leica) was used to examine and analyze the samples.

2.3 NMR theory

NMR is used to study the interaction between atomic nuclei and a magnetic field. The total NMR relaxation time (T_2) is associated with surface relaxation, bulk relaxation of fluid precession, and diffusion relaxation caused by the field gradient. Diffusion relaxation can be ignored when the applied electromagnetic field is uniform.

Therefore, the relationship between pore size and T_2 time can be established using a simple equation:

$$\frac{1}{T_2} = \rho \frac{S}{V} \quad (1)$$

The pore radius is proportional to the pore throat radius, thus Eq. (1) can be transformed into the following equation:

$$\frac{1}{T_2} = F_S \frac{\rho}{r} \quad (2)$$

where ρ is the surface relaxivity strength ($\mu m/ms$) and S/V is the surface area to volume ratio (specific surface area) of the pores (μm^{-1}). r is the pore radius (μm), F_s is a geometrical factor (F_s=3 for spherical pores and F_s=2 for columnar pores).

Since smaller pores have small radii, Eq. (2) shows that hydrogen in a smaller pore relaxes faster than in a larger pore [21]. Consequently, the T_2 distribution in core samples reflects the PSD. In other words, the T_2 distribution can be transformed into the PSD, where the smallest pores have the shortest relaxation time, and vice versa.

2.4 Random walk pore spectral dimension (RWPSD) algorithm

A binary image obtained from PM can be used to clearly observe the pore structure within samples. The water infiltration process in porous media can be regarded as a random walk of water in pores. Particles in a binary image walked randomly in pores to simulate the water infiltration process in our samples. The pore spectral dimension can be determined from the random walk algorithm results and subsequently used to evaluate the pore structure interconnectivity in the samples.

Fig. 3 shows a simplified particle random walk model. In order to ensure the walk length is close to actual physical transportation, this study made a few reasonable assumptions. Two walk rules were described as follows:

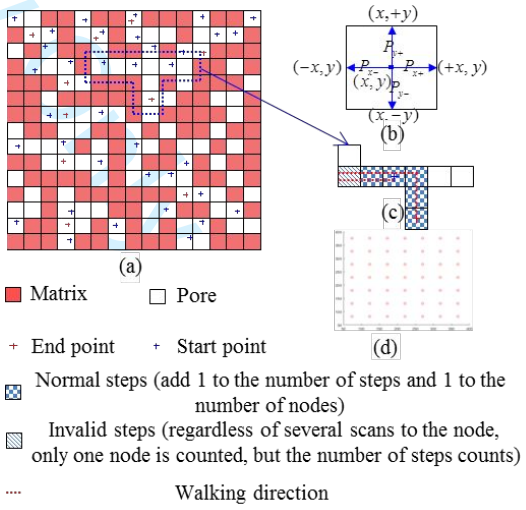

Fig. 3 Simplified particle random walk model in the pore; (b) particle walking direction and probability; (c) random walk process; (d) Ending point schematic diagram in a 7× 7 matrix.

(1) In order to ensure randomness of walking, 5000 particles used to be start points were randomly generated

in pores during a random walk. The end points were randomized to 49 within pores (Fig. 3). The particles walk from start points to end points was recorded as a valid walk within the prescriptive number of steps (10000).

(2) The particles only walked in pores, and the walking direction was randomly selected. In Fig.3(b), it can be seen that P_{x+}, P_{x-}, P_{y+}, and P_{y-} are the probability of walking in four adjacent direction and $P_{x+} = P_{x-} = P_{y+} = P_{y-} = 0.25$. After the particles collided with the matrix, they returned along their original path but in the opposite direction. Particles only walked one node (pixel) at a time. A duplicate node (Fig. 3c) in the path was marked as an invalid step. Regardless of the number of steps to the node, only one node was counted, but the number of steps counts.

The relationship between the number of different nodes P (area) that can be accessed and the number of walk steps (n) for 5000 particles in the binary image was as follows:

$$P \propto n^{d_s/2} \quad (3)$$

where d_s is the pore spectral dimension.

The definition of the pore spectral dimension objectively reflects the characteristics of pore shape and interconnectivity, and it establishes a bridge between pore structure, water permeation, and migration. It has been acknowledged that the pore spectral dimension in the pore structure can be used to quantitatively describe the complexity of the pore structure and correlates with the permeability of porous materials [22].

3. Results

3.1 Pore structure distributions obtained from NMR

Three or four peaks were observed in the NMR T_2 spectrum from the cement paste sample, where one or two peaks were larger than the remaining peaks (Fig. 4).

Mehta and Monteiro [23] classified water in hardened cement paste (Fig. 5) as chemically combined water (water that is an integral part of the microstructure of various cement hydration products), interlayer water (water associated with C-S-H structure), adsorbed water (water molecules physically adsorbed onto the solid surface under the influence of attractive forces), capillary water (water present in voids), and free water (water that exists in larger pores or cracks). Jeheng [24] measured the apparent transverse relaxation time of chemically combined water in the backfill to be 12 μs. Reports in the literature [24,25] also mention that the value of T_2 for chemically combined water is very short, and the CMPG experiment cannot be used to collect a signal from chemically combined water in the sample. Therefore, the four peaks in the T_2 spectrum correspond to NMR signals of interlayer water, adsorbed water, capillary water, and free water. One can see from Eq. (2) that T_2 is proportional to the pore radius. The radius of the pores containing interlayer water, adsorbed water, capillary water, and free water gradually increases. Thus, peaks p1, p2, p3, and p4 in Fig. 4 represent interlayer water, adsorbed water, capillary water, and free water, respectively. Peaks p3 and p4 was obvious in Fig. 4, while peaks p1 and p2 can cross or overlap.

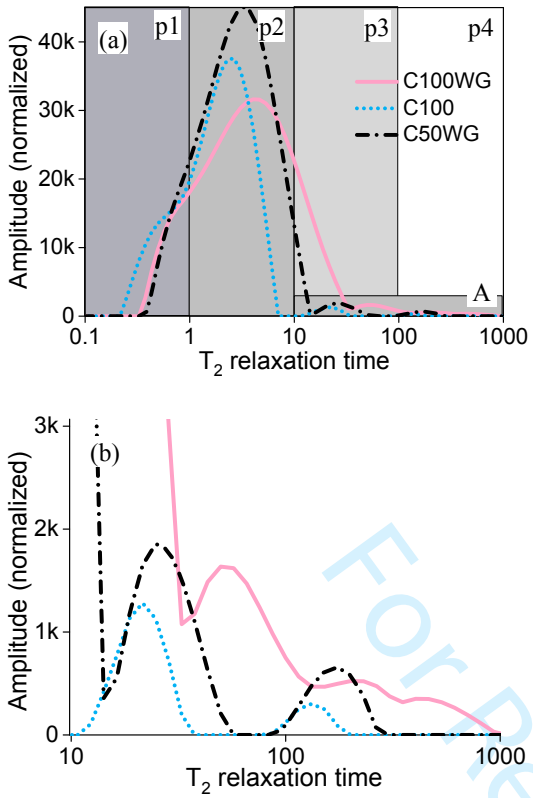

Fig. 4 T_2 relaxation time for three types of samples cured for 1 d. An enlarged view of area A is shown in (b).

The T_2 relaxation time spectrum has four typical peaks (p1), (p2), (p3), and (p4). The ratio of the areas occupied by peaks p1 and p2 in the T_2 spectrum of all samples reached more than 90%, which was the main peak in the NMR T_2 spectrum. This is the main source of relaxation signals. In particular, p2 showed the strongest signal intensity and the largest spectral area. The p2 spectral area in all samples covers p1 to a certain extent, especially in sample C50WG, where the p1 signal is almost completely contained in the p2 signal. Consequently, interlayer water and adsorbed water are the primary signal sources for transverse relaxation and showed the largest proportion for the four water types in all samples.

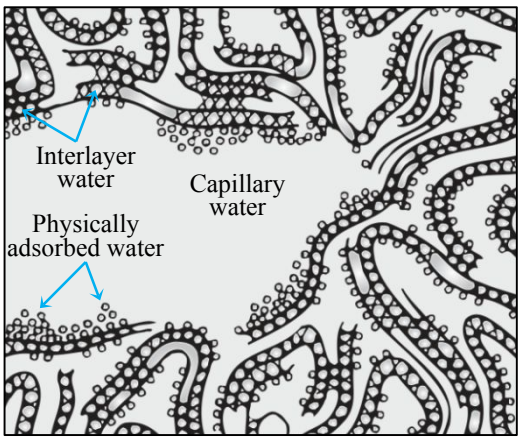

Fig. 5 Schematic diagram of cement material microstructure includes interlayer water, adsorbed water, and capillary water. Taken from Mehta and Monteiro [23].

Peaks p1 and p2 overlapped with each other in all experimental results, which indicated that there were overlaps and crossovers between interlayer water and adsorbed water in the geometric size distribution. Regarding interlayer water (Fig. 5), it has been suggested that a monomolecular water layer between C-S-H layers is strongly anchored by hydrogen bonding. Adsorbed water (Fig. 5) is water that is close to the solid surface. Water molecules physically adsorb onto the surface of solids in the hydrated cement paste under the influence of attractive forces. It has been suggested that up to six molecular layers of water can be physically anchored by hydrogen bonding.

Nevertheless, there are not always six molecular layers of water that physically adsorb onto the surface of solids. Some perturbation may cause water layers to break away, leaving less than six remaining water layers. There may be only one molecular layer of water. The geometric dimension between the adsorbed water and the

interlayer water appear to be similar, and the dividing line between the different states of water is not rigid at this time. Consequently, overlaps and crossovers between p1 and p2 are present in the NMR T_2 spectrum.

The transverse relaxation signal results show that water existed in the hydrated paste in the other two states, which produced a strong relaxation signal in addition to a large amount of water alongside interlayer water and adsorbed water. From the foregoing discussion of water in cement paste, the remaining water was capillary water (p3) and free water (p4) within voids in the hydrated paste. Free water has the longest T_2 relaxation time and the most unstable water content. In some tests, no signal is generated, thus there are only three peak signals. In the T_2 spectrum of the C100WG sample, the p3 and p4 peaks are also combined and are observed as a new peak (p3+p4). The p3 peak appeared to left shift, which indicates that the pores in the C50WG sample were larger. This indicates that the pores and fractures have similar geometric dimensions, as represented by intersection of the p3 and p4 peaks.

In addition to the peak areas, the relaxation time corresponding to the spectrum peak was another important characteristic parameter. The observed peaks are basically symmetric, and the peak maximum is located in the middle of spectrum peak. Accordingly, the relaxation time at the peak position can indicate changes in the pore size.

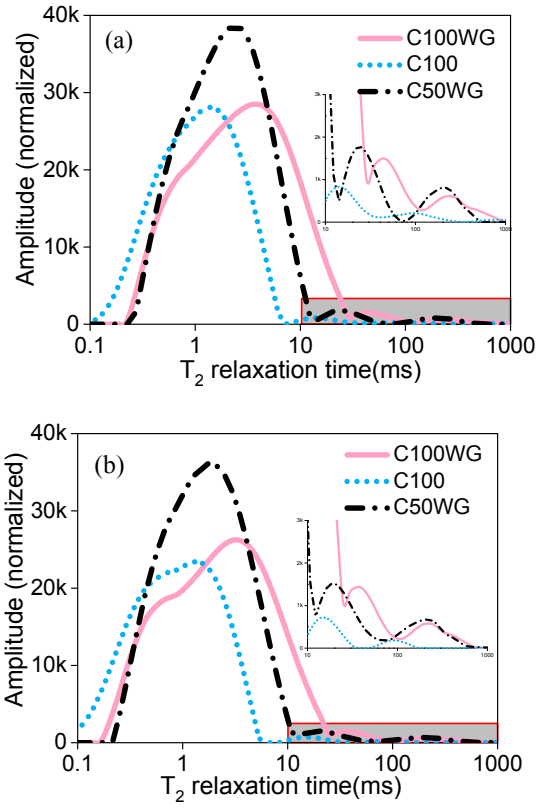

Fig. 6 T_2 relaxation time spectrum for three types of samples and local magnification of peaks 3 and 4. The curing time is (a) 7 d and (b) 28 d.

The NMR T_2 spectra for the three paste samples are shown in Fig. 6. There are some similarities among the T_2 peak values, peak positions, and peaks shapes for different curing times. It can be concluded by comparing the sample analysis results that the C100WG peak positions (p1+p2, p3 and p4) are at the far right, the C50WG peaks are in the middle, and the C100 peaks are at the far left. The C100WG samples exhibits a higher T_2 value, indicating more interlayer water, adsorbed water, capillary water, and free water voids. This reveals that the average pore size in the C100WG sample is larger.

The lowest p3 and p4 values of the C100 sample indicate that capillary water and free water content are

lowest, thus macro-pores did not develop and fracture did not occur. Peak p1 for the C50WG sample is the highest and most similar to C100, indicating that interlayer water is present in high proportion, and the distribution of micropores and mesopores is dense. The overlap between the p3 and p4 peaks in the C100WG sample indicates that there are cross-scale interconnected channels between the sample pores, which increases permeability to a certain degree.

3.2 Pore structure description through thin sections analysis

As previously mentioned, the different gray values between pores and mineral phases allow for separation of porosity from the solid grains by image analysis (IA) in terms of image capture and treatment. It is well known [24] that identifying the IA threshold (i.e., the critical grey level for binary segmentation) is critical in microstructural analysis of cemented materials. This important step is at the base of subsequent processing stages. This is particularly the case in this investigation, as binary images are used for more than one purpose (i.e., porosity evaluation, PSD, and pore interconnectivity) [25]. The C100WG and C50WG samples are known to have a high porosity, often above 40% (Fig. 12). Under this condition, it is relatively straightforward to evaluate a threshold value related to porosity in a histogram of grey levels.

Fig. 7 shows binary images from two topical samples (C100-3d and C100-7d). For such samples, the typical grey level curves are always bimodal, with one mode related exclusively to the solid phase (zone ‘‘C’’ in Fig. 7) and the second mode partially related to voids and to solids (zones ‘‘A’’ and ‘‘B’’, respectively). The grey levels in zone ‘‘A’’ are only associated with the epoxy resin, while zone ‘‘B’’ is seen as a transition zone showing the epoxy containing less or more interlaced solids. Other authors have observed such transition zones in cement pastes [39]. In additional, there are other types of tonal curves, such as (c), (d), (e), (f), and (g) in Fig. 11, which are unimodal. In this case, the threshold level (TL) is equal to GL_1 and GL_2 (defined below), which means there are no transition zones “B” in the sample, and only pore zones “A” and solids zones “C” are present.

In the present study, the threshold is determined as the average between the darker grey values occupying the highest proportion of the image (GL_1 in Fig. 7) and the lowest value of the valley which is between the two main family peaks (GL_2 value). This technique was validated using the total porosity of the three sample types. Implementation of an unambiguous, objective, and repeatable procedure to evaluate the threshold value is a key aspect in order to recognize and compare the evolution of the pore structure parameters over time and for different sample types. There are two grey level distribution models (unimodal and bimodal) in Fig.7. The X-axis represents the grey level (0~255), and the Y-axis represents number of pixels. The A, B, and C represent pore zone, transition zone, and solids zone, respectively. GL1 is the grey level at the beginning of the

zone A. GL2 is the grey level at the beginning of the zone C. The threshold level (TL) is equal to (GL1+GL2)/2.

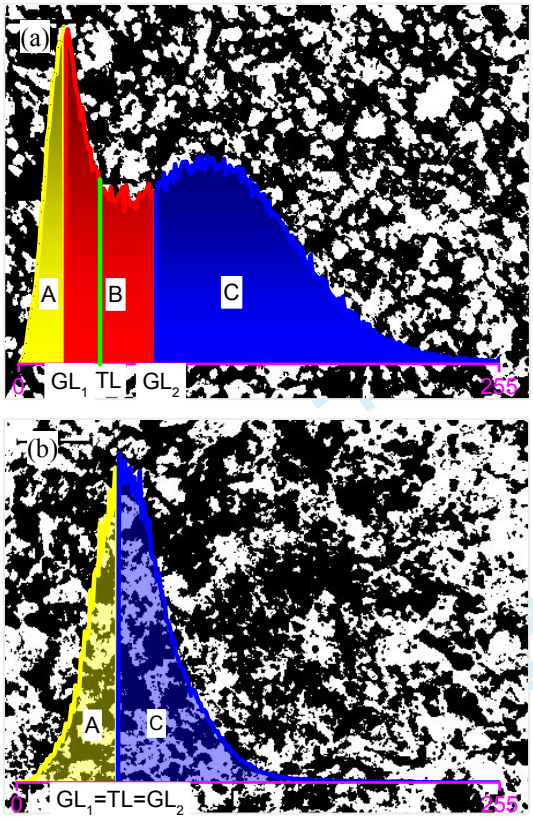

Fig. 7 Binary image obtained from the PM image.

Clear thin section images of the grouting samples were obtained using PM. Images for different curing times (3 d, 7 d, 14 d, and 28 d) are shown in Fig. 8. Thin section analysis of porous materials is primarily based on distinguishing grey levels in PM images with image processing software. In the PM mode, the grey level is directly proportional to the backscatter coefficient, which is related to the atomic number of the chemical elements. The mineral phases presenting the highest average atomic numbers are the brightest in the image with 256 grey levels. Because the epoxy resin used as a pore filling and stabilizing material mostly contains carbon (Z=6), the backscatter coefficient of the pores is low and the pixels representing the voids in the PM images are dark. Thus, various pores and fracture structures can be clearly observed.

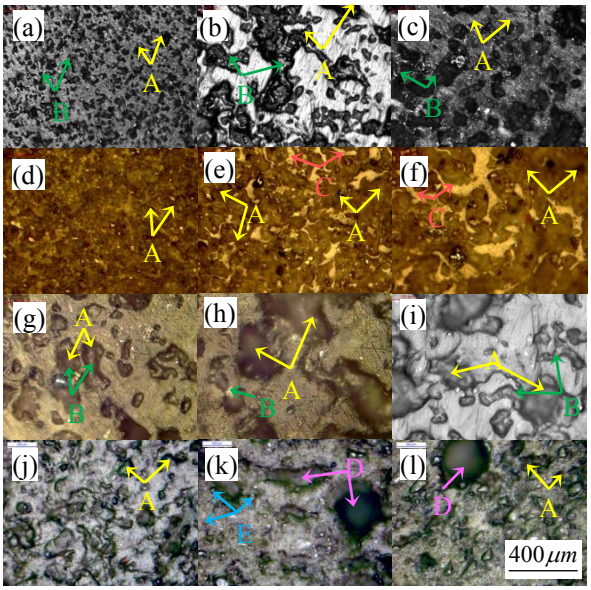

Fig. 8 Polarizing microscope images of the samples at 100× magnification. (a), (d), (g), and (j) indicate a curing time of 3 d, 7 d, 14 d, and 28 d for the C100 sample, respectively. (b), (e), (h), and (k) indicate the C100WG samples. (c), (f), (i), and (l) indicate the C50WG samples.

A, B, C, D, and E in Fig. 8 indicate pores, pore throats, hydration products, air holes and cracks and tailing particles. The three types of samples form a grid-like structure on the sample slice surface. The hydration reaction did not occur instantaneously in the paste. First, particulate matter aggregates in the paste to form particles with a certain size distribution. As the hydration reaction progresses, the hydration product nucleates and particles grow on the surface, which promotes formation of a porous structure resembling a neuron.

The C100 structure formed was the most compact (Fig. 8, C100). The C100WG sample hydrated product particles were connected to each other up to a size of 100 μm (Fig. 8(b), C100WG-3d), which constituted the coarser network structure and porous structure of the quick-setting paste. When the curing time reached 28 days, the C100WG compactness did not improve significantly (Fig. 8(k), C100WG-28d). Gaps in the structure were not significantly supplemented, nor were they strengthened by the hydration reaction process.

The structure of the C50WG sample is similar to the C100 and C100WG samples. The grid structure sizes in the C50WG sample is between the other two samples. Some of the tailings particles were completely encapsulated in hydration products and were distributed on the connection structure between the hydration products (Fig. 8(c), C50WG-3d), and the hydration products crystallize on the surface of the tailings particles. As the hydration reaction proceeds, many similarly rounded tailings particles are filled in the network structure of the C50WG sample (Fig. 8(l), C50WG-28d), which indicates that the tailings can fill gaps in a portion of the hydration product structure. This shows that tailings not only provide conditions for early hydration reactions, but they also improve the late hardening paste compactness.

There are a large number of pores in the skeletal grid of the hardening pastes, where the largest pore size reaches about 100 μm, while the smaller pore sizes are dozens of microns or even several microns. This occurs due to the hydration reaction. There are also some circular air holes with diameters of several hundred microns, which are the air bubbles resulting from the trapped air during the stirring process. In addition, there are crack structures in the C100WG and C50WG samples with unequal lengths and widths within dozens of microns. The air holes and cracks are large in size, and water can flow freely and damage the structure of these materials.

3.3 Setting time and UCS

The results showing initial setting time, final setting time, and UCS are shown in Fig. 9. The initial and final setting times of the pastes obviously increases with the presence of tailings. The initial and final setting times for C50 reached 7.43 and 29.58 min, respectively (Fig. 9a). For C50 and C50WG, i.e., in the pastes with tailings, the double-paste (main principal paste and water-glass paste) exhibits significantly reduced setting time. The double-paste has a slight effect on setting time in the C100 and C100WG pastes without tailings. The effect of the water-solid ratio of the pastes on the setting time is well known. In the C100WG sample, the water-glass paste can accelerate condensation, while it dilutes the pastes and retards time required for active particles in the cement to aggregate as solid structure. In the pastes with inert particles like tailings, the double-paste accelerates condensation more effectively, whereas the dilution effect is not obvious. Thus, the double-paste has a significant effect on the C50WG samples.

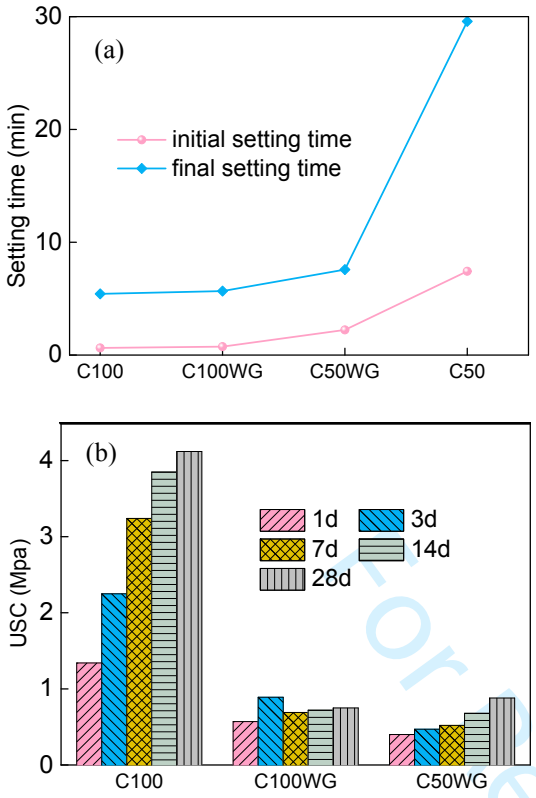

Fig. 9 (a) Initial setting and final setting time for three samples. The C50 samples are C50WG pastes without water-glass paste. (b) UCS for three samples.

As shown in Fig. 9b, the early strength increased significantly with the accelerator in the C100WG samples, but the development of later strength was reduced. The strength increased by only 0.06 Mpa over the 7 d to 28 d curing time. However, the strength of the C50WG sample with tailings grew steadily during the curing period. The strength of the C100 sample was larger than that of the other two samples, and the strength increased steadily and rapidly with curing time.

In the UCS tests, there are two primary failure modes that occur in grouting materials. One is the overall splitting and failure of the specimen (Fig.10a), while the other is the local failure at both ends (Fig.10b). According to the quick setting mechanism, one can infer that the effect of the accelerator is to transition from a local quick set process to the overall set process during quick setting. It also changes the chemical composition, and the preferential cement will consume calcium in the cement slurry. Therefore, the strength of the C100WG sample reached its maximum after curing for 7 d, and the strength dropped from 7 d to 14 d. The C100WG and C50WG samples formed an uneven material distribution internally. It shows a local failure mode when the weak belt is distributed at both ends (Fig. 10).

Observed from the fracture surface, although the section is smooth, there are many pores of different sizes in the cemented body (Figs. 10a and 10b). Deterioration of internal pore distribution is an important reason for the decreased UCS. The reason for its formation may be the air enclosed inside the test piece during casting. It may also be due to the natural development of gelation caused by the added accelerator.

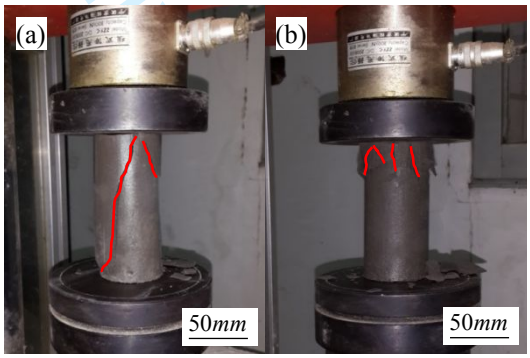

Fig. 10 (a) and (b) show destruction patterns for the uniaxial test in the C100WG and C50WG samples, respectively.

The accelerator causes the bubbles in the pastes to be discharged when the test piece is poured, resulting in a non-uniform pore distribution and poor strength.

However, the original quick-setting effect is slowed, the setting time is increased, the internal bubbles are discharged, and the internal pore distribution is improved due to the addition of tailings (Figs. 8 and 9). On the other hand, the accelerator will change the entire cementation process and hydration products, which will also have a certain impact on PSD. In summary, the accelerator would modify the hydration process and products, generate non-uniform pore structure, and increase porosity and pores interconnectivity, resulting in a reduced setting time and reduced strength during the later curing stage.

4. Discussions

4.1 Porosity

Fig. 11 shows binary images from all samples and the corresponding tonal curves presented in Fig. 8. The IA porosity obtained from binary IA and NMR porosity is shown in Fig. 12.

In the study of porous media such as rocks, the volume of water in porous media is regarded as the effective porosity according to Eq. (1). The NMR porosity of C100WG sample is largest, and the C100 sample NMR porosity is the smallest. The NMR porosity results are consistent with pore size and number obtained from the NMR T_2 spectra. The NMR porosity results for all three samples have negative correlations with curing time, as shown in Fig. 12. The NMR porosity of the C100, C50WG, and C100WG samples decreased from 33.7% to 24.9%, 49.0% to 42.541%, and 51.1% to 45.0%, respectively. The decreased amplitudes indicate that the former voids occupied by the evaporable water are gradually occupied by CH crystals, AFt crystals, and other substances produced by cement hydration. As a result, the total volume of all pores is reduced, and macropores gradually transform into micropores. At the same time, evaporable water is transferred to chemically combined water that exceeds the NMR detection range for the instrument used in this study.

The decreased proportion of evaporable water reveals the later hydration activity of the paste. The C100 pastes exhibited the highest reaction activity during the experimental observation period. However, the late-phase reaction activity of the paste samples must take into account conversion of evaporable water into chemically combined water and the physical conversion capacity among evaporable water states (interlayer water, adsorbed water, capillary water, and free water).

IA porosity has a negative correlation with curing time, which corresponds to the variation in NMR porosity. Nevertheless, the IA porosities obtained from IA are less than the NMR porosity for the same curing time. This occurs because distinguishability in PM is limited, and only the major pores with a certain size can be observed and distinguished. However, NMR can measure full-scale pores, including interlayer pores, gel pores, capillary pores, and fracture.

A previous study [26-28] found that the porosity for backfilling materials was less than 10%, in contrast with the results presented in this study. This is probably due to the different curing environment after the samples were

removed from the humidity chamber. A water environment increases water content in the samples and destroys the pore structure, thus changing the hydration reaction. This is detrimental for grouting materials to have a large porosity. In this condition, grouting materials will not play a role in plugging water. Fortunately, the inner pores are closed and do not interconnect with each other or external water environment. The pore spectral dimension and pore interconnectivity are used to verify our conclusion and quantify the pore interconnectivity in the next section.

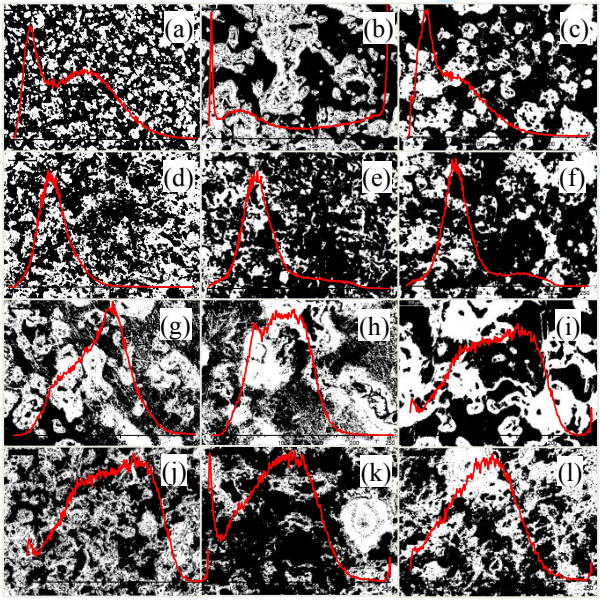

Fig. 11 Binary images and tonal curves for the images shown in Fig. 8; the sequence and scale are consistent with Fig. 8.

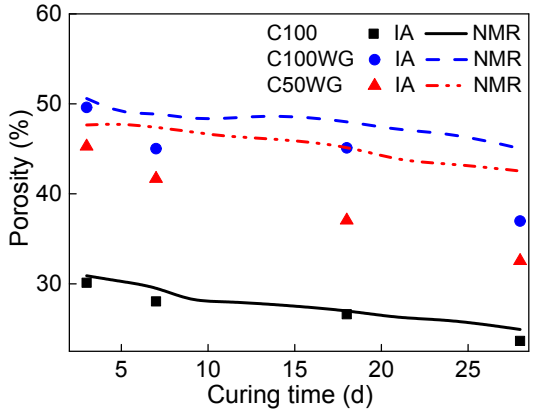

Fig. 12 The relationship between curing time and porosity. IA is the porosity calculated through image analysis, and NMR is the porosity obtained from NMR tests.

4.2 Pore spectral dimension and pore interconnectivity

The pore shapes and interconnectivity in the hardened pastes can be objectively determined from the pore spectral dimension (d_s), and the differential nodes P (area) corresponding to the same number of walk steps (n) was averaged. After calculating the logarithm of the number of walk steps and different nodes P, a series of plots are used to show the relationship between the number of walk steps and different nodes in all samples, as shown in Fig. 13.

Eq. (3) is used to fit a series of plots in Fig. 13 to obtain the pore spectral dimension (d_s) with correlation coefficients greater than 0.697, which verifies that the pore channel in porous media has fractal features.

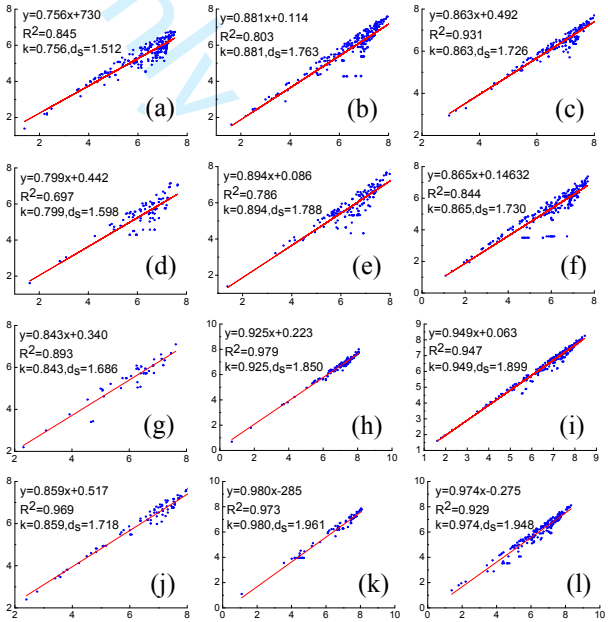

Fig. 13 RWPSD among all samples; the sequence is consistent

with Fig. 8.

In Fig. 13, the X axis is log n, where n is the number of steps in the random walk; the Y axis is log P, where P is different nodes or areas; R2 is correlation coefficient; k is equation slope; ds is pore spectral dimension. Previous studies have found that the pore spectral dimension in a porous structure is negatively correlated to the complexity of pore distribution structure and is positively correlated with pore interconnectivity. The pore spectral dimension value in the three kinds of samples follows the order C100WG>C50WG>C100 for the same curing time. This quantitatively shows that additional accelerators improve pore interconnectivity and mitigate complexity, which increases the rate of water penetration. The pore spectral dimension values for a given sample are positively correlated with curing time, indicating that pore interconnectivity increases and complexity decreases, while sample porosity also decreases (Figs. 12 and 13) as the hydration reaction proceeds. There seems to be some contradiction. In fact, the hydration reaction will increase the content of small and mesopores and reduce the number of macropores, which will increase interconnectivity. Nevertheless, the pore spectral dimension and interconnectivity show no obvious correlation with setting time.

As can be seen from Fig. 14, pore interconnectivity and NMR porosity are negatively correlated for a given sample, i.e., a larger pore porosity results in smaller pore interconnectivity. However, the relationship among C100, C100WG, and C50WG NMR porosity and pore interconnectivity exhibits the opposite rule, i.e., large NMR porosity corresponds to macropore interconnectivity.

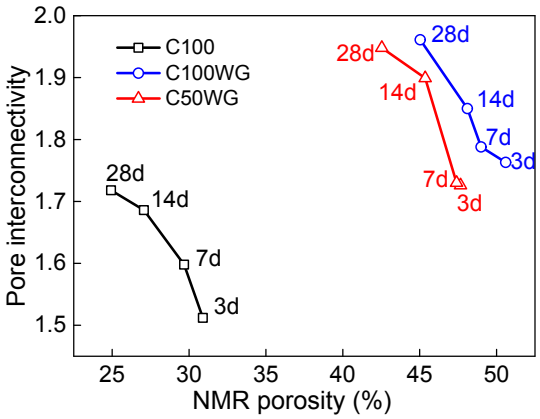

Fig. 14 Relationship between NMR porosity and pore interconnectivity.

When combined with the pore structure analysis (Fig. 8), one can deduce that the hydration reaction products gradually fill the macropores, which generates small pores and increases pore interconnectivity. The samples produced different pore structures due to the addition of accelerators, where a large resulting in a high number of micropores and large porosity. At this point, a large porosity value became a major factor affecting pore interconnectivity.

When calculating pore connectivity, a starting point is set at the left boundary and an ending point is set at the right boundary. After conducting 10 tests with 1000 particles per test at the starting point, we found that none of the particles reached the ending point. This result indicates that pore interconnectivity is very poor in these materials, and water molecules cannot easily migrate through the pore structure, even for materials with high

porosity.

4.3 Comparison of pore structure distribution (PSD) characteristics by NMR and IA

The T_2 signal from the NMR data is generated by resonance of H atoms in bound and free water. In other words, the T_2 signal can be regarded as the signal from water in the backfill. The pores with backfill are space that was not filled with solid phase. Electron microscope images show that voids in the hydrated cement paste appear to be empty. Within the water-saturated backfill body, many forms of water existed in the backfill corresponding to pores with different sizes. Some reports in the literature [23,29,30] suggest that the hydrated cement paste contains several types of voids which have an important influence on its properties. Interlayer pores in C-S-H form within the C-S-H structure, which is considered to be part of the solids in the hydrated cement paste. The width of interlayer pores varies from 0.5 *nm* to 2.5 *nm*. Gel pores form during polymerization of aluminosilicate gel during curing, which are defined to range from 0.005 to 0.01 *μm* based results from PC concrete research. Capillary pores contain the space not filled by solid components of the hydrated cement paste, which are defined to range from 0.01 to 5 *μm*. Air holes contain a small amount of air trapped in the cement paste during concrete mixing, the shape of which is generally spherical.

One can see from our contextual declaration that the four spectral peaks represent interlayer water, adsorbed water, capillary water, and free water. A given T_2 distribution corresponds to a given PSD, where each relaxation time corresponds to a pore size. A larger pore corresponds to a longer relaxation time, and vice versa for smaller pores. According to the literature[21] and Eq. (2), the relationship between relaxation time and pore radius can be obtained. The radius derived from the relaxation time in this study generally matches the range described above for four types of pores. Therefore, the four spectral peaks correspond to interlayer pores, gel pores, capillary pores, and fractures. The peak area and peak position of the T_2 relaxation time distribution (Figs. 4 and 6) statistics of p1+p2, p3, and p4 are shown in Fig. 15.

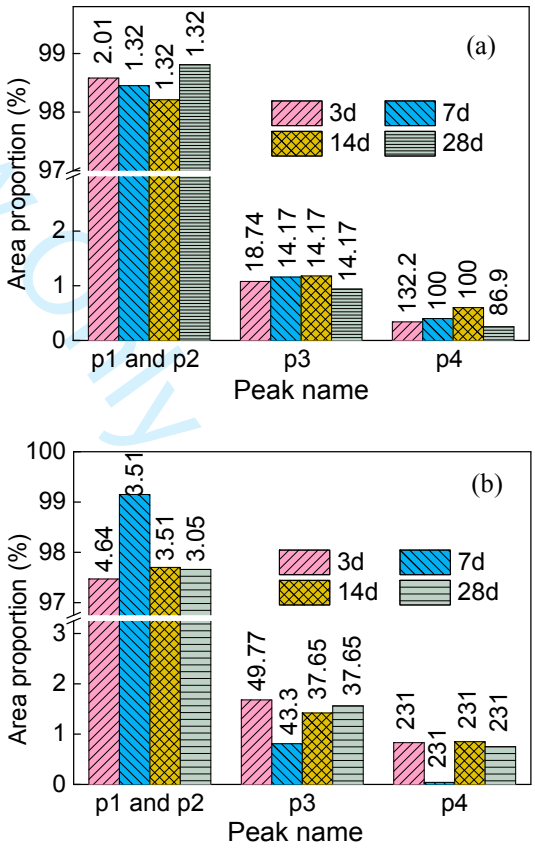

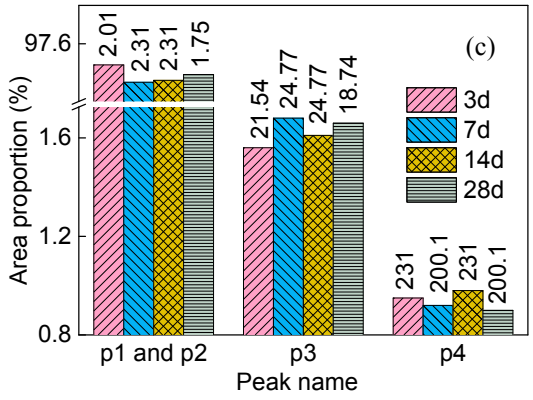

Fig. 15 Peak area proportion and peak position for (a) C100, (b) C100WG, and (c) C50WG. The values shown above the histogram are the peak positions corresponding to the T_2 relaxation time.

After curing for 3 days, the relaxation time for p1 in the C100 and C50WG samples was significantly lower than in the C100WG samples. This showed that the internal structure within the C50WG and C100 samples has higher density. The relaxation time gap for p2 between the C100, C50WG, and C100WG samples increased, which revealed that the pore size in each sample can be ordered C100WG > C50WG > C100.

After curing for 28 days, pores in the three samples continued to develop denser structures. These structures were different among the three samples, and each formed its own unique pore structure (Fig. 8).

The primary pore evolution characteristics are as follows: (1) pores became smaller and denser over time in all three samples. Difference in the pore sizes between the three samples increased as curing age increased. The C100 sample exhibited the fastest transformation rate of macropores and mesopores into micropores, followed by C50WG and C100WG. (2) Interlayer pore and gel pore content continuously increased, and capillary pore content decreased, as indicated by changes in the peak area changing during the curing process.

There are some differences in coagulation evolution mechanism among the three samples due to composition differences. This is an important process for improving the pore structure in a grouting material, requiring a conversion from capillary water to interlayer water and adsorbed water. The NMR results show that capillary water slowly and continuously converted into interlayer water and adsorbed water in the C100 samples. Meanwhile, the ratio of interlayer pores to gel pores in the C100WG sample was basically the same. We speculate that the incorporation of a quick-setting coagulant inhibits the original hydration process and blocks the transformation of capillary water into interlayer water and adsorbed water. This reveals that the C100WG samples had basically completed its entire hydration reaction during the early stage, after which the hydration reaction was very weak.

The interlayer water and adsorbed water content in the C50WG sample showed an increasing trend with curing time. The transition from capillary water to interlayer water and adsorbed water is evident. Although the incorporation of tailings in pastes retards the setting time and inhibits early activity to a certain extent, the active components in tailings played an important role in the later hydration reaction stage.

Grouting materials eventually formed porous media with different sizes as a main body. In terms of pore size,

the samples can be ordered C100WG > C50WG > C100.

5. Conclusions

(1) The experimental results show that the microstructure of the grouting materials used in this study consisted of interlayer pores, gel pores, capillary pores, circular air holes, and fractures. The T_2 spectra obtained from NMR analysis reflected four pore size distributions. However, the spatial size of the interlayer pores and gel pores was similar and only shows three distinct signal peaks. We can also conclude that capillary water can be converted to adsorbed water and interlayer water as curing time increases during sample preparation, and the ratio of gel pores to interlayer pores increased accordingly.

(2) Pore interconnectivity and curing time exhibited a positive correlation. For a given curing time, the samples can be ordered C100WG > C50WG > C100 in terms of pore interconnectivity. Pore interconnectivity and NMR porosity are negatively correlated for a given sample, i.e., a sample with larger NMR porosity has smaller pore interconnectivity. However, the relationship between C100, C100WG, and C50WG shows the opposite rule, namely that large NMR porosity corresponds to macropores interconnectivity.

(3) We also concluded from our results that an accelerator would change the hydration process and products, generate a non-uniform pore structure, and increase porosity and pore interconnectivity, resulting reduced setting time and reduced later strength.

(4) Tailings can fill gaps in a portion of the hydration product structure and densify the hydration products, thus overcoming any defects in a quick-setting slurry and reducing strength loss. This demonstrates that it is completely feasible to add tailings to the quick-setting slurry. Meanwhile, the grouting materials with added tailings allow tailings to be reused.

Reference

[1] WU Ai-xiang, LIU Chao, YIN Sheng-hua, XUE Zhen-lin, CHEN, Xun. Pore structure and liquid flow velocity distribution in water-saturated porous media probed by MRI[J]. Transactions of Nonferrous Metals Society of China, 2016, 26(5): 1403-1409

[2] FANG Xiang-qing, FU Yao-jun. Impact of karst water on coal mining in North China[J]. Environmental Geology, 2006, 49(3):449–457.

[3] SAKHAEE-POUR A, BRYANT S L. Effect of pore structure on the producibility of tight-gas sandstones[J]. Aapg Bulletin, 2014, 98(4):663-694.

[4] FOURMENTIN M, FAURE P, RODTS P, PETER U, LESUEUR D. NMR observation of water transfer between a cement paste and a porous medium[J]. Cement and Concrete Research, 2017, 95:56-64.

[5] ZUNINO F, BENTZ D P, CASTRO J. Reducing setting time of blended cement paste containing high-SO_3, fly ash (HSFA) using chemical/physical accelerators and by fly ash pre-washing[J]. Cement and Concrete Composition, 2018, 90:14-26.

[6] MALTESE C, PISTOLESI C, BRAVO A, CELLA F, CERULLI T, SALVIONI D. A case history: Effect of moisture on the setting behaviour of a Portland cement reacting with an alkali-free accelerator[J]. Cement and Concrete Research, 2007, 37(6):856-865.

[7] HIGGS K E, ZWINGMANN H, REYES A G, FUNNELL R H, DIAGENESIS, porosity evolution, and petroleum emplace- ment in tight gas reservoirs, Taranaki Basin, NewZea- land[J]. Journal of Sedimentary Research, 2007, 77(12): 1003−1025.

[8] WANG Xiao-hua, LI Jin-shan, HU Rui, KOU, Hong-chao. Mechanical properties and pore structure deformation behaviour of biomedical porous titanium[J]. Transactions of Nonferrous Metals Society of China, 2014, 24(3):

833-838.

[9] YANG Bao-hua, WU Ai-xiang, MIAO Xiu-xiu, LIU Jin-zhi. 3D characterization and analysis of pore structure of packed ore particle beds based on computed tomography images[J]. Transactions of Nonferrous Metals Society of China, 2015, 25(5): 1543-1550.

[10] SHANG Jun-long, HU Jian-hua, ZHOU Ke-ping, LUO Xian-wei, ALIYU M. Porosity increment and strength degradation of low-porosity sedimentary rocks under different loading conditions[J]. International Journal of Rock Mechanics and Mining Sciences, 2015, 75:216-223.

[11]SUN Xiao, ZHANG Bin, DAI Qing-li, YU Xiong. Investigation of internal curing effects on microstructure and permeability of interface transition zones in cement mortar with SEM imaging, transport simulation and hydration modeling techniques[J]. Construction and Building Materials, 2015, 76:366-379.

[12] FAVVAS E P, SAPALIDIS A A, STEFANOPOULOS K L, ROMANOS G E, KANELLOPOULOS N K, KARGIOT- IS E K, MITROPOULOS A C. Characterization of carbonate rocks by combination of scattering, porosimetry and permeability techniques[J]. Microporous and Mesoporous Materials, 2009, 120(1): 109-114.

[13] HU Jian-hua, REN Qi-fan, JIANG Quan, GAO Ru-gao, ZHANG Long, LUO Zhou-quan. Strength characteristics and the reaction mechanism of stone powder cement tailings backfill[J]. Advances in Materials Science and Engineering, 2018, 2018. DOI: https://doi.org/10.1155/2018/8651239.

[14] YAO Yan-Bin, LIU Da-Meng. Comparison of low-field NMR and mercury intrusion porosimetry in characterizing pore size distributions of coals[J]. Fuel, 2012,95(1):152-158.

[15]YANG Bao-hua, WU Ai-xiang, WANG Chun-lai, NIU Wen-xin, LIU Jin-zhi. Three-dimensional simulation of pore scale fluid flow in granular ore media with realistic geometry[J]. Transactions of Nonferrous Metals Society of China, 2012, 22(12): 3081-3086.

[16]MIZUSAWA K. Polarizing microscope observations of pottery from the Yashiro sites, Nagano Prefecture, Central Japan[J]. Quaternary International, 2016, 397:495-503.

[17] ZHOU San-dong, LIU Da-meng, CAI Yi-dong, YAO Yan-bin. Fractal characterization of pore–fracture in low-rank coals using a low-field NMR relaxation method[J]. Fuel, 2016, 181:218-226.

[18] YAO Yan-bin, LIU Da-meng, CHE Yao, TANG Da-zhen, TANG Shu-heng, HUANG Wen-hui. Petrophysical characterrization of coals by low-field nuclear magnetic resonance (NMR)[J]. Fuel, 2010, 89(7): 1371−1380.

[19] XU You-Wei. Application of directional random walk algorithm based on fractal method in the research of heat transfer in porous media[D]. Master's Thesis, Yangzhou University, Yangzhou, China, 2014. (in Chinese)

[20]CHEN Yong-ping, SHI Ming-heng. Determination of permeability for porous media using fractal theory[J]. Journal of Tsinghua University, 2000, 40(12)94-97.

[21] LI Jie-lin, LIU Han-wen, AI Kai-ming, ZHU Long-yin. An NMR-based experimental study on the pore structure of the hydration process of mine filling slurry[J]. Advances in Civil Engineering. 2018, 2018. DOI: https://doi.org/10.1155/2018/4720356.

[22] JI Yan-liang, SUN Zhen-ping, JIANG Xiao-xing, LIU Yi, SHUI Liang-liang, CHEN Chao. Fractal characterization on pore structure and analysis of fluidity and bleeding of fresh cement paste based on 1 H low-field NMR[J]. Construction and Building Materials, 2017, 140:445-453.

[23] MEHTA P K, MONTEIRO P J M. Concrete: microstructure, properties, and materials[M]. 2nd ed. McGraw-Hill Professional, 1993.

[24] JEHNG J. Microstructure of wet cement pastes: a nuclear magnetic resonance study[D]. Doctor's Thesis, Northwestern University, Evanston, USA, 1995.

[25] DAVY C A, ADLER P M. Three-scale analysis of the permeability of a natural shale[J]. Physical Review, 2017,96:1-12.

[24] OUELLET S, BUSSIERE B, AUBERTIN M, BENZAAZ-OUA M. Microstructural evolution of cemented paste backfill: mercury intrusion porosimetry test results[J]. Cement and Concrete Research, 2007,37(12): 1654-1665.

[25] OUELLET S, BUSSIERE B, AUBERTIN M, BENZAAZ-OUA M. Characterization of cemented paste backfill pore structure using SEM and IA analysis[J]. Bulletin of Engineering Geology and the Environment, 2008, 67 (2):139-152.

[26] GAO Ru-gao, ZHOU Ke-ping, LI Jie-lin. Research of the mechanisms of backfill formation and damage[J].

Materiali. Techno- logije, 2017, 52(2):163-169.

[27] ZHOU Ke-ping, GAO Ru-gao, GAO Feng. Particle flow characteristics and transportation optimization of superfine unclassified backfilling[J]. Mineral, 2017, 7(1):6-27.

[28] QI Chong-chong, FOURIE A, CHEN Qiu-song, TANG Xiao-lin, ZHANG Qin-li, GAO Ru-gao. Data-driven modelling of the flocculation process on mineral processing tailings treatment[J]. Journal of Cleaner Production, 2018, 196: 505-516.

[29] MANGAT P S, OJEDOKUN O O. Influence of curing on pore properties and strength of alkali activated mortars[J]. Construction and Building materials, 2018, 188: 337-348.

[30] SANTOS A R, VEIGA M D, SILVA A S, DE BRITO J. ALVAREZ J I. Evolution of the microstructure of lime based mortars and influence on the mechanical behaviour: The role of the aggregates[J]. Construction and Building materials, 2018, 187: 907-922.

矿用注浆材料宏细观跨尺度孔隙结构特征分析

胡建华[1]，任启帆[1]，马少维[1]，蒋权[1]，蒋元建[1]，尚俊龙[2]，罗周全[1]

1.中南大学 资源与安全工程学院，长沙 410083

2. 南洋理工大学 土木与环境工程学院 南洋地下空间中心，新加坡

摘 要：宏细观孔隙结构特征的跨尺度研究，有利于分析注浆材料的微观孔隙结构对其物理性能的影响。采取薄层断面分析和低场核磁共振（NMR）技术对三种类型注浆材料的微观孔隙结构和孔隙率进行表征，通过图像二值化和随机行走孔隙谱维数（RWPSD）算法量化注浆材料的宏观孔隙特征——孔隙贯通性。实验结果表明：（1）研究所用的注浆材料微观结构由层间孔、吸附孔、毛细孔、圆形气孔和微裂缝组成。尾矿可以充填在水化产物结构中的孔隙内，使水化产物更加致密。（2）孔隙贯通性与养护时间呈正相关，与孔隙率之间存在一定规律。（3）研究所用的有速凝剂的注浆材料，在存在不均匀的孔隙结构和增加孔隙率和孔隙贯通性时，会减少凝结时间和降低后期强度。

关键词：注浆材料；孔隙微观结构；孔隙贯通性；跨尺度研究；核磁共振；薄层断面分析；随机行走孔隙谱维数

Details in revision according to reviewer's comments and suggestions on the manuscript "Transactions of Nonferrous Metals Society of China TNMSC-2018-0658"

Title of paper: Macroscopic and microscopic trans-scale characteristics analysis of pore structure of mine grouting materials

Authors: Jian-hua HU*[1], Qifan REN, Quan Jiang[1], Yuan-jian JIANG[1], Jun-long SHANG[2], Zhou-quan LUO[1]

[1] Central south university, School of resources and safety engineering, Hunan Changsha 410083,China

* Correspondence: hujh21@csu.edu.cn

We addressed the comments of the reviewer (with green color) with responses as listed below, corresponding to necessary changes, additional sentences and short sections at proper places which are marked by blue color in the revised version of manuscript.

Reviewer: 1

Q1-(Reviewer): 文中把孔隙结构分为层间孔、吸附孔、毛细孔等，其中"吸附孔"的提法不正确。学术界从来没有"吸附孔"一说，只有"吸附水"之称。吸附水所在的孔更接近于水化产物的凝胶孔。

Response 1: I have consulted literature about the "absorbed pores" and "gel pores" and found that terminology of gel pores is usually used in academia to describe pores that are formed during the polymerization of aluminosilicate gel during curing. Additionally, the gel pores are defined to be within the range of 0.005–0.01 μm based on PC concrete research. The large capillary pores which are orders of magnitude bigger than gel pores and are within the range of 0.01–100 μm based on PC concrete research. Gel pores can express the connotation of absorbed pores defined by myself. So it is accurate to describe absorbed pores as gel pores in this paper. I have revised the expression. The revised sections are as follows:

Abstract: (1) the microstructure of the grouting materials used in the study consisted of interlayer pores, gel pores, capillary pores, circular air holes, and microfractures and tailings can fill some gaps in the hydration product structure and densify hydration products.

4.1 Porosity: IA porosity has a negative correlation with curing time, which corresponds to the variation in NMR porosity. Nevertheless, the IA porosities obtained from IA are less than the NMR porosity for the same curing time. This occurs because distinguishability in PM is limited, and only the major pores with a certain size can be observed and distinguished. However, NMR can measure full-scale pores, including interlayer pores, gel pores, capillary pores and fracture.

4.3 Comparison of pore structure distribution (PSD) characteristics by NMR and IA: Therefore, the four spectral peaks correspond to interlayer pores, gel pores, capillary pores, and

fractures. The peak area and peak position of the T2 relaxation time distribution (Figs. 4 and 6) statistics of p1+p2, p3, and p4 are shown in Fig. 15.

(2) Interlayer pore and gel pore content continuously increased, and capillary pore content decreased, as indicated by changes in the peak area changing during the curing process.

There are some differences in coagulation evolution mechanism among the three samples due to composition differences. This is an important process for improving the pore structure in a grouting material, requiring a conversion from capillary water to interlayer water and adsorbed water. The NMR results show that capillary water slowly and continuously converted into interlayer water and adsorbed water in the C100 samples. Meanwhile, the ratio of interlayer pores to gel pores in the C100WG sample was basically the same. We speculate that the incorporation of a quick-setting coagulant inhibits the original hydration process and blocks the transformation of capillary water into interlayer water and adsorbed water. This reveals that the C100WG samples had basically completed its entire hydration reaction during the early stage, after which the hydration reaction was very weak.

In the section 4.3, I redefined the pores within the backfill and illustrated the characteristic for each type of pores. Meanwhile the relationship between T_2 signals, water and pores is expressed. The revised section is as follows:

4.3 Comparison of pore structure distribution (PSD) characteristics by NMR and IA: The T2 signal of NMR is generated by resonance of H atoms in bound and free water. In other words T2 signal can be regarded as the signal of water in the backfill. The pores with backfill are the space not filled by solid phase. Under electron microscopic examination, voids in the hydrated cement paste appear to be empty. Within water-saturated body of backfill， many forms of water existed in backfill corresponds to pores with different spatial sizes. Some literatures[23,29,30] suggest that the hydrated cement paste contains several types of voids which have an important influence on its properties. Interlayer pores in C-S-H are formed within the C-S-H structure which is considered as a part of the solids in the hydrated cement paste. The width of interlayer pores varies from 0.5 nm to 2.5 nm. Gel pores are formed during the polymerization of aluminosilicate gel during curing, which are defined to be within the range of 0.005~0.01 μm based on PC concrete research. Capillary pores represent the space not filled by the solid components of the hydrated cement paste which are defined to be within the range of 0.01~5 μm. Air holes are a small amount of air trapped in the cement paste during concrete mixing, the shape of which is generally spherical.

According to the literature[21], the relationship between relaxation time and pore radius can be obtained. The radius derived by relaxation time in this study general match the range described above for four types of pores.

References:

[29] MANGAT P S, OJEDOKUN O O. Influence of curing on pore properties and strength of alkali activated mortars[J]. Construction and Building materials, 2018, 188: 337-348.

[30] SANTOS A R, VEIGA M D, SILVA A S, DE BRITO J. ALVAREZ J I. Evolution of the microstructure of lime based mortars and influence on the mechanical behaviour: The role of the aggregates[J]. Construction and Building materials, 2018, 187: 907-922.

Q2-(Reviewer):论文 3.1 中，将 T_2 谱峰根据弛豫时间 0.1-1ms,1-10ms,10-50ms,50-1000ms 的不同范围分别对应层间水，吸附水，毛细水，自由水，这种划分依据略显不足，主观性较强，似乎有意识选取了整数数量级作为划分的分界点。而根据 2.3 核磁理论来说，似乎应该建立孔隙尺寸和弛豫时间之间的关系更为准确。而且，论文作者引用的 Metha 等人的著作中，对不同状态的水及其所在孔隙的尺寸亦有交代。

Response 2: I have reviewed the related literatures about the criterion to divide relaxation time into different forms of water in water-saturated backfill. However there is no distinct expression about the size of pores or water. For example in the book “Concrete: Microstructure, Properties, and Materials”, Mehta et al. suggest that capillary water is the water present in voids larger than about 5 nm, adsorbed water up to six molecular layers of water (1.5 nm) can be physically held by hydrogen bonding, and a monomolecular water (0.25 nm) of interlayer water layer between the layers of C-S-H is strongly held by hydrogen bonding. Meanwhile the width of interlayer pores varies from 0.5 nm to 2.5 nm. Capillary pores represent the space not filled by the solid components of the hydrated cement paste which are defined to be within the range of 0.01~5 μm. Sidney Mindess et al. repeal that the gel pores are defined to be within the range of 0.005–0.01 μm based on PC concrete research. The large capillary pores which are orders of magnitude bigger than gel pores and are within the range of 0.01~100 μm based on PC concrete research. Yao et al. demonstrate that NMR T_2 distributions for 100% water-saturated samples are commonly bimodal, unimodal and multimodal, with peaks of adsorption pores (<0.1 μm) at 0.5~2.5 ms, seepage pores (>0.1 μm) at 20~50 ms, and the cleats (or fractures) at >100 ms. Li et al. suggest the aperture range as follws:

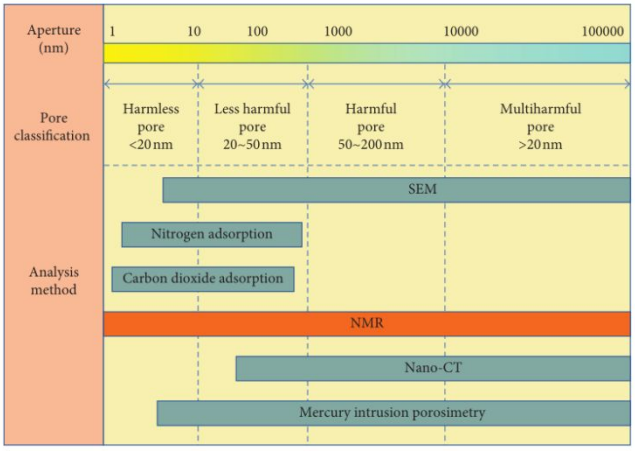

Figure.1 Aperture ranges (nm) for filling slurry pore properties' characterization methods
According to literature[21], the relationship between the pore radius

and T_2 can be expressed as:

$$r = 24T_2 \times 10^{-9}$$

where r is pore radius; T_2 is relaxation time.

By the criterion of Metha et al. the value of dividing for capillary water, adsorbed water and interlayer water should be 0.021ms, 0.0625ms, and 0.0104ms. Obviously this conclusion is unreasonable. If this was true, the T_2 would almost not have signals, because the relaxation time of adsorbed water and interlayer water exceed the measurement range of NMR equipment. For many scholars, it is acceptable that adsorbed water and interlayer water can be measured by using NMR. Similarly the value of dividing for capillary pores and interlayer pores should be 0.021~0.104ms and 0.417~208ms. For the criterion Sidney Mindess, the value of dividing for gel pores and capillary pores should be 0.208~0.417ms and 0.417~4166ms.

What I mean by this is that the dividing criterion is not uniform, which results in that the conclusion is unreliable. In addition the relationship between pore radius and relaxation time is also inaccurate, because too many assumptions are used to derive the formula.

In the section 3.1, what I want to express is water in different bound states corresponding to each peak. I do not focus on the dividing citation for T_2 relaxation time of each form of bound states. Additionally this study doesn't attach that much attention on this problem. Thus my suggestion is that we should avoid referring this controversial content in this article. According to your suggestion, the relationship between pore radius and T_2 relaxation time has been built. The revised section is as follows:

In section 2.3 NMR theory: Therefore, the relationship between pore size and T2 time can be established using a simple equation:

$$\frac{1}{T_2} = \rho \frac{S}{V} \quad (1)$$

The pore radius is proportional to the pore throat radius, so Eq. (1) can be transformed into the following equation:

$$\frac{1}{T_2} = F_S \frac{\rho}{r} \quad (2)$$

where ρ is the surface relaxivity strength ($\mu m/ms$); S/V is the surface area to volume ratio (specific surface area) of the pores (μm^{-1}). r is the pore radius(μm); F_S is a geometrical factor (for the spherical pores, $F_S = 3$; for the columnar pores, $F_S = 2$).

Since smaller pores have minor radius values, Eq. (2) shows that hydrogen proton in smaller pores relaxes faster than that in a larger pore [21]. Consequently, the T_2 distribution in core samples reflects the PSD. In other words T_2 distribution can be transformed into the PSD, with the smallest pores having the shortest relaxation time, and vice versa.

In section 3.1 Pore structure distributions obtained from NMR: Jeheng measured the apparent transverse relaxation time of the chemically combined water in the backfill to be 12 μm. Literatures also show that the value of T_2 relaxation time of chemically combined water is very short, and the CMPG experiment cannot collect the signal of chemically combined water in the sample. Therefore, the four peaks of the T_2 spectrum correspond to the NMR signals of interlayer water, adsorbed water, capillary water and free water. It can be seen from Eq. 2 that the T_2 relaxation time is proportional to pore radius. The radius of the pores where interlayer water, adsorbed water, capillary water, and free water exist gradually increases. Thus the peaks of p1, p2, p3 and p4 respectively represent interlayer water, adsorbed water, capillary water and free water.

References:

[21] LI Jie-lin, LIU Han-wen, AI Kai-ming, ZHU Long-yin. An NMR-based experimental study on the pore structure of the hydration process of mine filling slurry[J]. Advances in Civil Engineering. 2018, 2018:0-12. https://doi.org/-10.1155/2018/4720356.

[23] MEHTA P K, MONTEIRO P J M. Concrete: micro- structure, properties, and materials[M]. 2nd ed. McGraw- Hill Professional, 1993.

[29] MANGAT P S, OJEDOKUN O O. Influence of curing on pore properties and strength of alkali activated mortars[J]. Construction and Building materials, 2018, 188: 337-348.

[30] SANTOS A R, VEIGA M D, SILVA A S, DE BRITO J. ALVAREZ J I. Evolution of the microstructure of lime based mortars and influence on the mechanical behaviour: The role of the aggregates[J]. Construction and Building materials, 2018, 187: 907-922.

D. Sidney Mindess, J. Francis Young, Darwin, Concrete, Prentice Hall, Pearson Education, Inc., Upper Saddle River, NJ 07458, U.S.A.,, 2003.

Q3-(Reviewer): Introduction 部分"mercury porosimetry"应该是"mercury intrusion porosimetry (MIP)"

Response 3: I have revised the "mercury porosimetry" to "mercury intrusion porosimetry (MIP)" in the introduction section. The revised section is as follows:

Many techniques have been applied to investigate the pore characteristics of concrete materials in previous studies, such as environmental scanning microscopy[8], X-ray computer tomography scanning[9], nuclear magnetic resonance(NMR)[10], scanning electron microscopy(SEM)[11], and mercury intrusion porosimetry(MIP)[12].

Details in revision according to editor's comments and suggestions on the manuscript "Transactions of Nonferrous Metals Society of China TNMSC-2018-0658"

Title of paper: Macroscopic and microscopic trans-scale characteristics analysis of pore structure of mine grouting materials

Authors: Jian-hua HU*[1], Qifan REN, Quan Jiang[1], Yuan-jian JIANG[1], Jun-long SHANG[2], Zhou-quan LUO[1]

[1] Central south university, School of resources and safety engineering, Hunan Changsha 410083,China

* Correspondence: hujh21@csu.edu.cn

We addressed the comments of the editor (with green color) with responses as listed below, corresponding to necessary changes, additional sentences and short sections at proper places which are marked by red color in the revised version of manuscript.

Q1: A concise and factual abstract is required. It should contain the objective, methods, results and conclusions, with emphasis on the results and conclusions.

Response 1: The revised abstract are as follows:

This paper presents a laboratory description of the microstructure of grouting materials in terms of pore structure and interconnectivity. Pore structure was characterized based on a thin-section analysis and low-field nuclear magnetic resonance (NMR) technique. A macroscopic study of pore interconnectivity was then quantified from a binary image captured with a thin-section analysis and random walk pore spectral dimension (RWPSD) algorithm. The experimental results show that: (1) the microstructure of the grouting materials used in the study consisted of interlayer pores, gel pores, capillary pores, circular air holes, and fractures and tailings can fill some gaps in the hydration product structure and densify hydration products. (2) there is a positive correlation between pore interconnectivity and curing time. In addition, there is a relationship between pore interconnectivity and porosity. (3) A non-uniform pore structure generating, and porosity and pore interconnectivity increasing of the samples with accelerator result reduced setting time and reduced later strength.

Q2: Make sure you use uniform letter and size of your original artwork.

Response 2: The uniform letter and size of the original artwork have been used.

Q3: The style of the references should be arranged according to the following examples.

Response 3: The style of the references has been arranged according to the examples. I have referred the relevant literatures published in "Transactions of Nonferrous Metals Society of China". The revised references are as follows:

[1] WU Ai-xiang, LIU Chao, YIN Sheng-hua, XUE Zhen-lin, CHEN, Xun. Pore structure and liquid flow velocity distribution in water-saturated porous media probed by MRI[J]. Transactions of Nonferrous Metals Society of China, 2016, 26(5): 1403-1409

[8] WANG Xiao-hua, LI Jin-shan, HU Rui, KOU, Hong-chao. Mechanical properties and pore structure deformation behaviour of biomedical porous titanium[J]. Transactions of Nonferrous Metals Society of China, 2014, 24(3): 833-838.

[9] YANG Bao-hua, WU Ai-xiang, MIAO Xiu-xiu, LIU Jin-zhi. 3D characterization and analysis of pore structure of packed ore particle beds based on computed tomography images[J]. Transactions of Nonferrous Metals Society of China, 2015, 25(5): 1543-1550.

[15]YANG Bao-hua, WU Ai-xiang, WANG Chun-lai, NIU Wen-xin, LIU Jin-zhi. Three-dimensional simulation of pore scale fluid flow in granular ore media with realistic geometry[J]. Transactions of Nonferrous Metals Society of China, 2012, 22(12): 3081-3086.

已经按照《初审表》意见进行修改。修改的部分在文章中用红色字体表示，删减的部分没有做标记。

Details in revision according to editor's comments and suggestions on the manuscript "Transactions of Nonferrous Metals Society of China TNMSC-2018-0658"

Title of paper: Macroscopic and microscopic trans-scale characteristics of pore structure of mine grouting materials

Authors: Jian-hua HU[1], Qifan REN[1], Shao-wei MA[1*], Quan Jiang[1], Yuan-jian JIANG[1], Jun-long SHANG[2], Zhou-quan LUO[1]

[1] Central south university, School of resources and safety engineering, Hunan Changsha 410083,China

* Correspondence: mashaowei@csu.edu.cn

1. 照片/线图中文字的字号、字体请参照本刊格式，照片中文字建议采用可修改的浮动的文本框格式.

答：已按照贵刊的格式要求将图片中文字的大小改为"新罗马 10 号字体"，图例说明字体为"新罗马 9 号"。精简和修改了部分的图题说明。

2. 英文中不得使用中文特殊符号，如③，等等。

答：文章中的中文特殊符号已经全部删除，替换为英文符号。

3. 参考文献中部分文献存在错误。

答: 参考文献中的错误已经修改，其中有部分的开源期刊没有固定的参考文献格式，故将文章的 DOI 放上。